Inorganic Chemistry

ARTICLE

pubs.acs.org/IC

Reversible and Irreversible Vapor-Induced Guest Molecule Exchange in Spin-Crossover Compounds

Rong-Jia Wei, Jun Tao,* Rong-Bin Huang, and Lan-Sun Zheng

State Key Laboratory of Physical Chemistry of Solid Surfaces and College of Chemistry and Chemical Engineering, Xiamen University, Xiamen 361005, People's Republic of China

S Supporting Information

ABSTRACT: Spin-crossover (SCO) complex $[Fe(tpa)(NCS)_2]$ (tpa = tri(2-pyridylmethyl)amine) crystallized in two solvate forms, yellow $[Fe(tpa)(NCS)_2]\cdot X$ [Fe:X = 1:1; X = *n*-PrOH (complex is named as ***n*-PrOH**), *i*-PrOH (***i*-PrOH**), CH_2Cl_2 (**CH_2Cl_2**), $CHCl_3$ (**$CHCl_3$**), MeCN (**MeCN**)] and red $[Fe(tpa)(NCS)_2]_2\cdot Y$ [Fe:Y = 2:1; Y = MeOH (**MeOH**), EtOH (**EtOH**)], respectively. Between the two forms, interesting solvent-vapor induced in situ reversible and irreversible guest molecule exchanges, $[Fe(tpa)(NCS)_2]\cdot X \rightleftharpoons [Fe(tpa)(NCS)_2]_2\cdot Y$, occurred in the solid state followed by dramatic color changes as well as distinct structural and SCO behavior transformations. Comprehensive studies on structures and SCO behaviors associating guest exchanges have been conducted by X-ray single-crystal diffraction, PXRD, IR, elemental analysis, and magnetic measurements, respectively. This discrete molecular system shows unique solvent-dependent SCO behavior related to the nature of solvent molecules; the distinct color changes during guest exchange originate from the alternations of electronic states of the guest-sensitive Fe^{II} centers, providing an effective route to fine-tune and optimize materials' properties by systematic structural perturbation, or serving for detection of toxic gases, such as CH_2Cl_2 and $CHCl_3$.

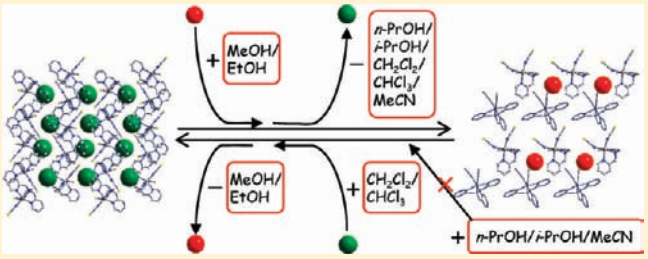

INTRODUCTION

Construction of porous complexes in the crystalline state has become a highly active interdisciplinary research area over the past decades.[1] Ordered cavities and channels provided by porous complexes could be rationally designed and controlled, allowing guest molecules, typically gases and solvent molecules, to be absorbed and reside, which render them promising applications such as gas storage,[2] selective guest sorption,[3] and sensors.[4] Recently, some metal coordination complexes exhibiting unique structural changes induced by removal/readsorption of guest molecules in a crystal-to-crystal transformation are reported.[5] Those structural dynamics through cooperative solid state transformation are appealing, especially those with reversibility, which provides a deeper understanding of the correlation between unique physicochemical properties and crystal structures at atomic level.[6] However, it is still a challenge, especially for those transformations between discrete molecular crystals, of which crystallinity is difficult to maintain following the rearrangement of molecules in the solid state.[7] Indeed, with the exceptions of a few examples,[8] crystalline transformation to achieve close packing upon guest exchange is almost observed for organic molecular crystals,[9] as well as for coordination networks.

In addition to understanding and controlling structural features, considerable effort has been explored in obtaining molecular crystals with unique properties in the area of catalysis,[10] magnetism,[11] and luminescence,[12] originating from the selective encapsulations within the inner channels and cavities of a self-assembled molecular container. In terms of applications, the control of spin-crossover (SCO) properties is an important issue, in which the high-spin (hs) and low-spin (ls) states are interconvertible upon change of conditions such as temperature and pressure, and the resulting molecular bistability renders SCO complexes useful for futuristic applications such as the development of miniature molecule-based display devices or data storage elements.[13] Up to now, more than 200 SCO systems have been reported in literature reports.[14] Over the course of these studies, it has been clear that guest molecules, mainly solvent molecules, can drastically affect the SCO behaviors of iron(II) complexes.[15] In fact, encapsulation of guest molecules significantly changes intermolecular cooperative interactions such as $\pi-\pi$ stacking, hydrogen bonding, and van der Waals contacts that play important roles in tuning the ligand-field strength and crystal packing and in enhancing bistable behavior.[16] Considerable efforts have thus been made to explore the solvent influences on SCO behavior in the solid state by changing crystallization guests.[17] In most cases, these guest-incorporated materials cocrystallize with solvent molecules from solution driven by the principle "nature abhors a vacuum".[18] The first successful control of SCO behavior in the solid state, however, was only recently reported by Kepert and co-workers in 2002,[19] in which the nanoporous coordination framework $[Fe_2(azpy)_4(NCS)_4]\cdot(guest)$ (azpy = *trans*-4,4′-azopyridine) undergoes spin transition that is influenced

Received: May 28, 2011
Published: July 27, 2011

by reversible exchange of guest solvent molecules. Through this pioneering work, a new avenue for investigating SCO phenomena in the solid state is explored, with solvent exchange as a convenient means for perturbing the crystal packing structure, and, therefore, the SCO properties. Since then, a small number of SCO systems displaying solvent-exchange process have been reported,[19−21] in which most of the exchanges[19,20] are explored following desorption by heating samples and subsequent sorption in the associating guest vapor, with only one exception[21] that in situ exchange took place without the process of desorption.

We have recently reported the complex $[Fe(tpa)(NCS)_2]$ (Figure 1, polymorphs **I**−**IV**)[22] and its (p**I**) interesting methanol vapor-induced single crystal-to-single crystal transformation behavior, which not only changes the crystal structure generating a new complex $[Fe(tpa)(NCS)_2]_2 \cdot MeOH$ (**MeOH**), but also dramatically alters the SCO behavior.[22c] The rather open and flexible packing structure of p**I** prompted us to consider other solvent molecules, which may perturb the cooperative interactions in the solid state and modify the properties of spin transition. We have found that p**I** could recrystallize in five different solvents to give similar yellow forms with a Fe^{II}:guest ratio of 1:1, $[Fe(tpa)(NCS)_2] \cdot X$ [X = *n*-PrOH (complex is named as ***n*-PrOH**), *i*-PrOH (***i*-PrOH**), CH_2Cl_2 (**CH_2Cl_2**), $CHCl_3$ (**$CHCl_3$**), MeCN (**MeCN**)]. Besides that, when immersed in liquid ethanol, the p**I** crystals could directly transform to the ethanol-incorporating species with a Fe^{II}:guest ratio of 2:1, $[Fe(tpa)(NCS)_2]_2 \cdot EtOH$ (**EtOH**), which has a red color at room temperature similar to that of **MeOH**,[22c] here denoted as $[Fe(tpa)(NCS)_2]_2 \cdot Y$ (Y = MeOH or EtOH). What is interesting is that, between the two solvate crystal forms, solvent-vapor induced in situ reversible and irreversible guest molecule exchanges, $[Fe(tpa)(NCS)_2] \cdot X \rightleftharpoons [Fe(tpa)(NCS)_2]_2 \cdot Y$ (Figure 2), which occurred in the solid state followed by dramatic color changes as well as distinct structural and SCO behavior transformations. As expected, solvent dependence of SCO behavior was established (see Magnetic Properties section), and the seven solvated complexes, therefore, provide a perfect system through which a solvent effect on SCO could be explored. The investigation of such transformation is significant because it can provide not only unique properties characteristic of discrete molecule crystals, but also external stimulus-responsive properties based on the vapor-induced solvent exchange, such as serving for detection of toxic gases or tuning magnetic properties on the molecular scale, a long sought-after goal in bistable material research.

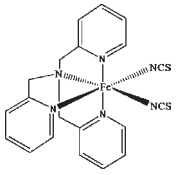

Figure 1. Molecular structure of $[Fe(tpa)(NCS)_2]$.

EXPERIMENTAL SECTION

Materials and Physical Measurements. All starting materials were obtained commercially and were used without further purification. Elemental analyses for C, H, and N were performed on Perkin-Elmer 240Q elemental analyzer. The IR spectra (KBr pellets) were recorded in the range 400−4000 cm^{-1} on a Nicolet 5DX spectrophotometer. Powder X-ray diffraction (PXRD) studies were performed on Panalytical X-Pert PRO diffractometer with Cu Kα radiation (λ = 0.154 18 nm, 40.0 kV, 30.0 mA). Magnetic susceptibility measurements were carried out on a Quantum Design MPMS XL7 magnetometer at a sweeping rate of 1 K min^{-1} in the 2−390 K temperature range under magnetic field of 5000 Oe. Magnetic data were calibrated with the sample holder, and diamagnetic corrections were estimated from Pascal's constants.

Synthesis. Crystals of p**I**, p**IV**, and **MeOH** were prepared by literature methods.[22] Yellow crystals of p**I** immersed in a DMSO/ethanol (v/v = 1:5) mixture for two days gave red crystals of **EtOH** suitable for single-crystal analysis. Yield: 90%. Elemental analysis calcd (%) for $C_{42}H_{42}N_{12}Fe_2OS_4$: C 51.92, N 17.30, H 4.46. Found: C 51.66, N 17.68, H 4.06. IR (KBr, cm^{-1}): 3442, 2099, 2076, 2063, 1601, 1571, 1481, 1438, 766.

Single crystals of ***n*-PrOH**, ***i*-PrOH**, **CH_2Cl_2**, and **$CHCl_3$** were prepared by diffusing 1 mL of DMF solution of p**I** to the corresponding solvents, respectively.

***n*-PrOH.** Yield: 60%. Elemental analysis calcd (%) for $C_{23}H_{26}FeN_6OS_2$: C 52.87, N 16.09, H 5.02. Found: C 52.81, N 16.34, H 5.13. IR (KBr, cm^{-1}): 3458, 2073, 2058, 1602, 1571, 1478, 1438, 757.

***i*-PrOH.** Yield: 65%. Elemental analysis calcd (%) for $C_{23}H_{26}FeN_6OS_2$: C 52.87, N 16.09, H 5.02. Found: C 52.78, N 16.27, H 4.87. IR (KBr, cm^{-1}): 3443, 2072, 2054, 1602, 1572, 1478, 1439, 757.

CH_2Cl_2. Yield: 50%. Elemental analysis calcd (%) for $C_{63}H_{60}Cl_6Fe_3N_{18}S_6$: C 46.09, N 15.36 H 3.68. Found: C 46.43, N 15.43, H 3.87. IR (KBr, cm^{-1}): 3448, 2073, 2057, 1602, 1571, 1478, 1439, 757.

$CHCl_3$. Yield: 40%. Elemental analysis calcd (%) for $C_{42}H_{38}Cl_6Fe_2N_{12}S_4$: C 43.36, N 14.45 H 3.29. Found: C 43.40, N 14.36, H 3.03. IR (KBr, cm^{-1}): 3464, 2076, 2063, 1602, 1572, 1478, 1440, 756.

Yellow crystals of **MeCN** were obtained by immersing 50 mg of powder of p**I** in 1 mL of acetonitrile for 5 h. Yield: 40%. Elemental analysis calcd (%) for $C_{22}H_{21}FeN_7S_2$: C 52.49, N 19.48, H 4.20. Found: C 52.30, N 19.26, H 4.32. IR (KBr, cm^{-1}): 3432, 2099, 2064, 1601, 1571, 1480, 1438, 766, 758.

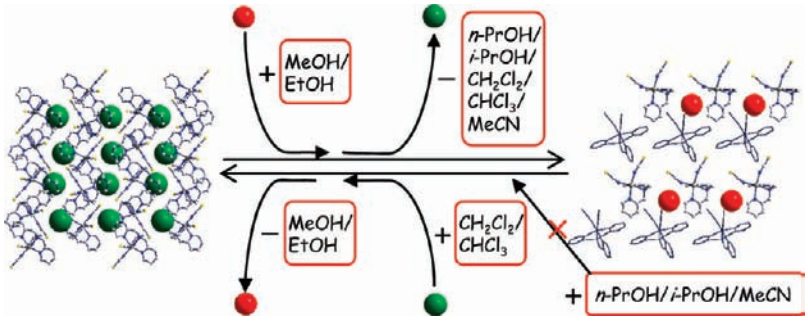

Figure 2. Schematic representation of structural transformation between crystals $[Fe(tpa)(NCS)_2] \cdot X$ (left) and $[Fe(tpa)(NCS)_2]_2 \cdot Y$ (right) triggered by specific solvent vapor. Red ball: MeOH or EtOH molecule. Green ball: *n*-PrOH, *i*-PrOH, MeCN, CH_2Cl_2, or $CHCl_3$ molecule.

Table 1. Crystal Data and Structure Refinements for EtOH, *n*-PrOH, and MeCN

	EtOH	EtOH	EtOH	*n*-PrOH		MeCN
formula	$C_{42}H_{42}Fe_2N_{12}OS_4$	$C_{42}H_{42}Fe_2N_{12}OS_4$	$C_{42}H_{42}Fe_2N_{12}OS_4$	$C_{23}H_{26}FeN_6OS_2$	$C_{23}H_{26}FeN_6OS_2$	$C_{22}H_{21}FeN_7S_2$
fw/g mol^{-1}	970.82	970.82	970.82	522.47	522.47	503.43
cryst syst	triclinic	triclinic	triclinic	monoclinic	monoclinic	orthorhombic
space group	$P\bar{1}$	$P\bar{1}$	$P\bar{1}$	$P2_1/c$	$P2_1/c$	$P2_12_12_1$
T/K	295	230	150	240	104	150
a/Å	9.611(2)	9.5388(4)	9.4671(5)	12.3008(8)	12.134(2)	11.656(2)
b/Å	15.727(2)	15.6249(7)	15.5262(8)	11.9241(8)	11.987(2)	13.043(2)
c/Å	16.174(3)	15.9598(8)	15.8017(9)	17.692(1)	16.925(2)	15.381(2)
α/deg	74.41(1)	74.567(4)	74.795(5)			
β/deg	88.30(1)	88.397(4)	88.664(4)	92.704(5)	90.137(17)	
γ/deg	76.72(1)	76.520(4)	76.191(5)			
V/Å^3	2290.4(6)	2228.3(2)	2174.7(2)	2592.0(3)	2461.8(8)	2338.3(6)
Z	2	2	2	4	4	4
D_c/g cm^{-3}	1.408	1.442	1.483	1.339	1.41	1.43
μ/mm^{-1}	0.863	0.887	0.909	0.769	0.810	0.848
reflns collected	18 585	17 758	20 853	13 042	10 839	6786
R1 ($I > 2\sigma(I)$)[b]	0.0448	0.0468	0.044	0.0416	0.0913	0.0384
wR2 (all data)	0.1233	0.1188	0.0767	0.0621	0.116	0.0501

[b] $R1 = ||F_o| - |F_c||/|F_o|$; $wR2 = \{[w(F_o^2 - F_c^2)^2]/[w(F_o^2)^2]\}^{1/2}$; $w = 1/[\sigma_2(F_o^2) + (ap)^2 + bp]$, where $p = [\max(F_o^2, 0) + 2F_c^2]/3$; and $Rw = [w(|F_o| - |F_c|)^2/w|F_o|^2]^{1/2}$, where $w = 1/\sigma^2(|F_o|)$.

The seven solvated complexes can be divided into two groups: the Fe^{II}:guest ratio is 2:1 for **MeOH** and **EtOH** and 1:1 for ***n*-PrOH**, ***i*-PrOH**, **CH_2Cl_2**, **$CHCl_3$**, and **MeCN**, respectively.

Vapor-Induced Guest Exchange and Transformation. Crystals of ***n*-PrOH**, ***i*-PrOH**, **CH_2Cl_2**, **$CHCl_3$**, and **MeCN** exposed in methanol vapor produced crystals of complex **MeOH**. Elemental analysis calcd (%) for $C_{41}H_{40}N_{12}OS_4Fe_2$: C 51.47, N 17.57 H 4.21. Found: C 51.62, N 18.03, H 4.03 for ***n*-PrOH → MeOH**; C 51.59, N 17.82, H 3.98 for ***i*-PrOH → MeOH**; C 51.61, N 17.71, H 3.94 for **CH_2Cl_2 → MeOH**; C 51.72, N 17.84, H 3.96 for **$CHCl_3$ → MeOH**; C 51.74, N 18.05, H 3.92 for **MeCN → MeOH**.

Crystals of ***n*-PrOH**, ***i*-PrOH**, **CH_2Cl_2**, **$CHCl_3$**, and **MeCN** exposed in ethanol vapor produced crystals of complex **EtOH**. Elemental analysis calcd (%) for $C_{42}H_{42}Fe_2N_{12}OS_4$: C 51.96, N 17.31, H 4.36. Found: C 51.56, N 17.48, H 4.69 for ***n*-PrOH → EtOH**; C 51.75, N 17.58, H 4.51 for ***i*-PrOH → EtOH**; C 51.89, N 17.80, H 4.11 for **CH_2Cl_2 → EtOH**; C 52.14, N 17.59, H 4.21 for **$CHCl_3$ → EtOH**; C 52.17, N 17.65, H 4.39 for **MeCN → EtOH**.

The exposure of **MeOH** and **EtOH** crystals in CH_2Cl_2 vapor produced complex **CH_2Cl_2**. Elemental analysis calcd (%) for $C_{63}H_{60}Cl_6Fe_3N_{18}S_6$: C 46.09, N 15.36 H 3.68. Found: C 46.22, N 15.45, H 3.74 for **MeOH → CH_2Cl_2**; C 46.00, N 15.28, H 3.59 for **EtOH → CH_2Cl_2**.

The exposure of **MeOH** and **EtOH** crystals in $CHCl_3$ vapor produced complex **$CHCl_3$**. Elemental analysis calcd (%) for $C_{42}H_{38}Cl_6Fe_2N_{12}S_4$: C 43.36, N 14.45 H 3.29. Found: C 43.66, N 14.58, H 3.43 for **MeOH → $CHCl_3$**; C 43.70, N 14.54, H 3.51 for **EtOH → $CHCl_3$**.

Crystallographic Data Collection and Structure Determination. Diffraction data of solvate crystals obtained from crystallization and solvent exchange were collected on Oxford Gemini S Ultra and Rigaku IP diffractometers using graphite monochromated radiation Mo Kα (λ = 0.710 73 Å). The crystal structures were solved and refined using the SHELXTL program suite.[23] Direct methods yielded all nonhydrogen atoms, which were refined anisotropically, while all hydrogen atom positions were calculated geometrically and were riding on their respective atoms. Crystallographic data and structural refinement details are presented in Tables 1, 2, 3 and 4. Selected bonds distances and parameters showing salient features of structures are summarized in Tables 5, 6, and 7.

RESULTS AND DISCUSSION

Solvent Exchange. Dynamically reversible guest exchange between the yellow crystals of **CH_2Cl_2** and **$CHCl_3$** and red crystals of **MeOH** and **EtOH** occurred in the associating solvent vapors, while the exchanges from ***n*-PrOH**, ***i*-PrOH**, and **MeCN** to **MeOH** and **EtOH** are irreversible, as presented in Figure 3. For example, by exposing crystals of **CH_2Cl_2** to methanol vapor, vivid color change from yellow to red occurred via a mixed yellow and red state within a few hours. The crystallagraphic data are the same as those of **MeOH** isolated from p**I** after absorbing methanol molecules, confirming the solvent-exchange reaction from **CH_2Cl_2** to **MeOH**. Furthermore, the yellow color can be recovered by exposing the red crystals of **MeOH** transformed from **CH_2Cl_2** to methylene chloride vapor again. Unfortunately, the crystallinity after two-step exchanges was poor, and no further structural data could be obtained for comparison. Similar crystallinity decay was also observed while exposing the red crystals of **MeOH** and **EtOH** to chloroform vapor. However, the structures after two-step exchanges are consistent with those of single-crystal **CH_2Cl_2** and **$CHCl_3$**, as evidenced by elemental analysis, PXRD (Figure 4), and magnetic studies (see below). We noted that the packing patterns of complex $[Fe(tpa)(NCS)_2]$ molecules in crystal structures of ***n*-PrOH**, ***i*-PrOH**, **CH_2Cl_2**, **$CHCl_3$**, and **MeCN** are essentially similar to that of p**I**, in which the channels between the complex units provide spaces for solvent molecules to reside, while those of complex $[Fe(tpa)(NCS)_2]$ molecules in crystal structures of **MeOH** and **EtOH** resemble that of p**IV**, another polymorph of $[Fe(tpa)(NCS)_2]$,[22d] providing cavities between distinct Fe_A and Fe_B complex units that are occupied by the molecules of methanol and ethanol for **MeOH** and **EtOH**, respectively (see Crystallographic Studies section). It appears that the solvent molecules, by replacing the original guests residing in the void space and participating in hydrogen-bond interactions with the complex molecules, help change the packing system. These solvent exchange approaches are

Table 2. Crystal Data and Structure Refinements for *i*-PrOH, CH_2Cl_2, and $CHCl_3$

	i-PrOH	*i*-PrOH	CH_2Cl_2	CH_2Cl_2	$CHCl_3$	$CHCl_3$
formula	$C_{23}H_{26}FeN_6OS_2$	$C_{23}H_{26}FeN_6OS_2$	$C_{63}H_{60}Cl_6Fe_3N_{18}S_6$	$C_{63}H_{60}Cl_6Fe_3N_{18}S_6$	$C_{42}H_{38}C_{l6}Fe_2N_{12}S_4$	$C_{42}H_{38}C_{l6}Fe_2N_{12}S_4$
M_r/g mol^{-1}	522.47	522.47	1641.96	1641.96	1163.48	1163.48
cryst syst	monoclinic	monoclinic	orthorhombic	orthorhombic	monoclinic	monoclinic
space group	$P2_1/c$	$P2_1/c$	$Pna2_1$	$Pna2_1$	$P2_1/c$	$P2_1/c$
T/K	240	104	240	104	240	104
a/Å	12.3112(7)	12.0961(7)	12.1038(4)	11.8609(4)	17.7299(5)	17.4450(5)
b/Å	11.9321(6)	12.0174(7)	17.6596(6)	17.0392(6)	12.3466(3)	12.2726(4)
c/Å	17.840(1)	16.9756(9)	35.107(1)	35.140(1)	23.2982(6)	23.1066(7)
α/deg						
β/deg	93.000(5)	90.370(5)			92.809(2)	93.138(3)
γ/deg						
V/Å^3	2617.1(3)	2467.6(2)	7504.0(5)	7101.8(4)	5093.9(2)	4939.6(3)
Z	4	4	4	4	4	4
D_c/g cm^{-3}	1.326	1.406	1.453	1.536	1.517	1.565
μ/mm^{-1}	0.762	0.808	1.005	1.061	1.093	1.127
reflns collected	9991	9824	41 256	40 183	24 766	22 534
R1 ($I > 2\sigma(I)$)[a]	0.0501	0.0428	0.0651	0.0643	0.0366	0.0298
wR2 (all data)	0.1123	0.0747	0.1354	0.0966	0.0673	0.0454

[a] R1 = $\|F_o| - |F_c\|/|F_o|$; wR2 = $\{[w(F_o^2 - F_c^2)^2]/[w(F_o^2)^2]\}^{1/2}$; $w = 1/[\sigma_2(F_o^2) + (ap)^2 + bp]$, where $p = [\max(F_o^2, 0) + 2F_c^2]/3$; and $Rw = [w(|F_o| - |F_c|)^2/w|F_o|^2]^{1/2}$, where $w = 1/\sigma^2(|F_o|)$.

Table 3. Crystal Data and Structure Refinements for MeOH exchanged from *n*-PrOH, *i*-PrOH, CH_2Cl_2, $CHCl_3$, and MeCN

	n-PrOH → MeOH	*i*-PrOH → MeOH	CH_2Cl_2 → MeOH	$CHCl_3$ → MeOH	MeCN → MeOH
formula	$C_{41}H_{40}Fe_2N_{12}OS_4$	$C_{41}H_{40}Fe_2N_{12}OS_4$	$C_{41}H_{40}Fe_2N_{12}OS_4$	$C_{41}H_{40}Fe_2N_{12}OS_4$	$C_{41}H_{40}Fe_2N_{12}OS_4$
M_r/g mol^{-1}	956.79	956.79	956.79	956.79	956.79
cryst syst	triclinic	triclinic	triclinic	triclinic	triclinic
space group	$P\bar{1}$	$P\bar{1}$	$P\bar{1}$	$P\bar{1}$	$P\bar{1}$
T/K	173	173	173	173	173
a/Å	9.4352(2)	9.4181(4)	9.4151(8)	9.4294(3)	9.4095(4)
b/Å	15.4950(3)	15.4782(5)	15.477(1)	15.4867(4)	15.4557(8)
c/Å	15.7576(3)	15.7959(5)	15.769(1)	15.7576(5)	15.7604(6)
α/deg	74.1050(7)	74.253(1)	74.190(2)	74.1870(8)	74.290(4)
β/deg	87.8170(7)	87.812(1)	87.815(2)	87.8800(9)	88.008(3)
γ/deg	75.8720(7)	75.857(1)	75.824(2)	75.8640(8)	75.899(4)
V/Å^3	2147.62(7)	2148.1(1)	2142.5(3)	2145.9(1)	2138.7(2)
Z	2	2	2	2	2
D_c/g cm^{-3}	1.48	1.479	1.483	1.481	1.486
μ/mm^{-1}	0.919	0.919	0.922	0.920	0.923
reflns collected	29 556	18 601	18 457	29 502	16 200
R1 ($I > 2\sigma(I)$)[b]	0.0291	0.0387	0.0748	0.0352	0.0431
wR2 (all data)	0.0375	0.0581	0.1460	0.0535	0.0648

[a] Most crystals after guest exchange could not show high-quality diffraction patterns, but the unit cells are almost the same as those of **MeOH** and **EtOH**, respectively. In fact, only several small crystals or part cut from large crystals could be used to collect diffraction data. In order to obtain good diffraction data, the exchange was performed by immersing crystals of ***n*-PrOH**, ***i*-PrOH**, **CH_2Cl_2**, **$CHCl_3$**, and **MeCN** in liquid MeOH and EtOH, respectively. [b] R1 = $\|F_o| - |F_c\|/|F_o|$; wR2 = $\{[w(F_o^2 - F_c^2)^2]/[w(F_o^2)^2]\}^{1/2}$; $w = 1/[\sigma_2(F_o^2) + (ap)^2 + bp]$, where $p = [\max(F_o^2, 0) + 2F_c^2]/3$; and $Rw = [w(|F_o| - |F_c|)^2/w|F_o|^2]^{1/2}$, where $w = 1/\sigma^2(|F_o|)$.

different from those in extended network structures,[5,19−21] whose frameworks are sufficiently rigid and often changed little upon solvent exchange reactions. Also, the distinct color changes during the exchange processes which originate from the alternations of the electronic states of Fe(II) centers suggest that it may be possible to alter and even better to fine-tune the properties (transition temperature, width of hysteresis loop) of SCO complexes by in situ control of guest molecules in the solid state.

Magnetic Properties. The $\chi_M T$ versus T plots for **EtOH** are shown in Figure 5. At a first glance, complex **EtOH** undergoes a one-step-like complete spin transition. At 390 K, the complex is in hs state with a $\chi_M T$ value of 6.915 cm^3 K mol^{-1}, corresponding to two paramagnetic hs-Fe^{II} ions. Upon cooling, the value

Table 4. Crystal Data and Structure Refinements for EtOH exchanged from *n*-PrOH, *i*-PrOH, CH_2Cl_2, $CHCl_3$, and MeCN[a]

	n-PrOH → EtOH	*i*-PrOH → EtOH	CH_2Cl_2 → EtOH	$CHCl_3$ → EtOH	MeCN → EtOH
formula	$C_{42}H_{42}Fe_2N_{12}OS_4$	$C_{42}H_{42}Fe_2N_{12}OS_4$	$C_{42}H_{42}Fe_2N_{12}OS_4$	$C_{42}H_{42}Fe_2N_{12}OS_4$	$C_{42}H_{42}Fe_2N_{12}OS_4$
M_r /g mol^{-1}	970.82	970.82	970.82	970.82	970.82
cryst syst	triclinic	triclinic	triclinic	triclinic	triclinic
space group	$P\bar{1}$	$P\bar{1}$	$P\bar{1}$	$P\bar{1}$	$P\bar{1}$
T/K	173	173	173	173	173
a/Å	9.4332(4)	9.4336(3)	9.4575(6)	9.4447(3)	9.4637(5)
b/Å	15.4690(8)	15.4804(7)	15.5206(6)	15.4813(7)	15.5046(6)
c/Å	15.8597(7)	15.8263(8)	15.8031(5)	15.8293(5)	15.7993(8)
α/deg	74.868(1)	74.839(4)	74.855(3)	74.860(3)	74.902(4)
β/deg	88.594(1)	88.610(3)	88.762(4)	88.659(3)	88.762(4)
γ/deg	76.187(2)	76.199(4)	76.249(4)	76.182(3)	76.232(4)
V/Å^3	2167.7(2)	2164.6(2)	2172.9(2)	2167.6(1)	2171.9(2)
Z	2	2	2	2	2
D_c/g cm^{-3}	1.487	1.49	1.484	1.48	1.484
μ/mm^{-1}	0.912	0.913	0.910	0.912	0.910
reflns collected	18 774	16 544	22 961	16 701	17 050
R1 ($I > 2\sigma(I)$)[b]	0.0622	0.0469	0.0622	0.0668	0.0509
wR2 (all data)	0.0994	0.1001	0.0953	0.1048	0.0727

[a] Most crystals after guest exchange could not show high-quality diffraction patterns, but the unit cells are almost the same as those of **MeOH** and **EtOH**, respectively. In fact, only several small crystals or part cut from large crystals could be used to collect diffraction data. In order to obtain good diffraction data, the exchange was performed by immersing crystals of ***n*-PrOH**, ***i*-PrOH**, **CH_2Cl_2**, **$CHCl_3$**, and **MeCN** in liquid MeOH and EtOH, respectively. [b] $R1 = ||F_o| - |F_c||/|F_o|$; $wR2 = \{[w(F_o^2 - F_c^2)^2]/[w(F_o^2)^2]\}^{1/2}$; $w = 1/[\sigma_2(F_o^2) + (ap)^2 + bp]$, where $p = [\max(F_o^2, 0) + 2F_c^2]/3$; and $Rw = [w(|F_o| - |F_c|)^2/w|F_o|^2]^{1/2}$, where $w = 1/\sigma^2(|F_o|)$.

Table 5. Selected Bond Lengths and Structural Parameters of pIV, MeOH, and EtOH at Various Temperatures

	pIV	MeOH	EtOH	EtOH	EtOH
T/K	150	120	295	230	150
$\langle d_{FeA\text{-}N}\rangle$/Å	1.959	1.957	2.118	2.015	1.962
$\langle d_{FeB\text{-}N}\rangle$/Å	1.967	1.963	2.146	2.06	1.965
Σ_A/Σ_B/deg	43.4/41.2	42.8/40.9	85.7/89.5	61.4/63.6	46.3/41.4
$\pi-\pi$ distance	4.038(2)/	4.340(4)/	4.655(1)/	4.437(2)/	4.352(1)/
within Fe_A/Fe_B layers/Å	4.298(2)	4.004(2)	4.283(1)	4.332(2)	4.428(2)
S···H−C distance within Fe_A layer/Å	2.975(1)	2.822(2)	2.949(2)	2.939(1)	2.913(2)
S···H−C distance within Fe_B layer/Å	2.853(1)	2.715(3)	3.030(1)	2.927(1)	2.841(2)
S···H−C distance between Fe_A and Fe_B layers/Å	2.692(1)	2.994(2)	2.835(1)	2.784(1)	2.759(1)
S···H−O distance/Å		2.537(2)	2.900(1)	2.860(2)	2.316(1)

Table 6. Selected Bond Lengths and Structural Parameters of pI, *n*-PrOH, and *i*-PrOH at Various Temperatures

	pI	*n*-PrOH	*n*-PrOH	*i*-PrOH	*i*-PrOH
T/K	260	240	104	240	104
$\langle d_{Fe-N}\rangle$/Å	2.168	2.167	1.977	2.166	1.974
Σ/deg	96.3	98.4	50.6	99.9	51.6
$\pi-\pi$ distance/Å	3.987(3)	3.917(2)	3.968(1)	3.903(2)	3.919(2)
S···H−C distance within 1D chain/Å	2.944(3)	2.920(2)	2.831(2)	2.955(1)	2.871(1)
S···H−C distance between 1D chains/Å	3.016(2)	2.925(2)	2.908(2)	2.988(1)	2.911(1)
S···H−O distance/Å		2.685(1)	2.548(1)	2.720(2)	2.521(1)

remains constant until 360 K, then drops continuously and reaches a value of 0.106 cm^3 K mol^{-1} at 174 K, implying a ls state. The $T_{1/2}$ is 242 K. The isostructural complex **MeOH**[22c] and their mother complex **pIV**[22d] (similar complex-packing style) have previously been reported, exhibiting two-step spin transitions with critical temperature of 303 ($T_{1/2(1)}$), and 230 K ($T_{1/2(2)}$), and 293 ($T_{1/2(1)}$) and 229 K ($T_{1/2(2)}$), respectively, are also shown in Figure 5 for comparison.

Complex ***n*-PrOH** shows a continuous and complete one-step SCO behavior. The $\chi_M T$ value undergoes a gradual decrease

Table 7. Selected Bond Lengths and Structural Parameters of CH_2Cl_2, $CHCl_3$, and MeCN at Various Temperatures

	CH_2Cl_2	CH_2Cl_2	$CHCl_3$	$CHCl_3$	MeCN
T/K	240	104	240	104	150
$\langle d_{FeA\text{-}N}\rangle$/Å	2.174	1.966	2.168	2.087	2.167
$\langle d_{FeB\text{-}N}\rangle$/Å	2.152	1.984	2.174	2.171	
$\langle d_{FeC\text{-}N}\rangle$/Å	2.157	1.969			
Σ(A/B/C)/deg	96.2/	49.4/	94.0	77.6/	105.4
	98.1/95.1	55.0/47.6	101.3/	101.4	
$\pi-\pi$ distance/Å	4.047(1)/3.943(1)	4.047(1)/3.947(1)	3.938(1)	3.950(1)	3.826(1)
S···H−C distance within 1D chain/Å	2.904(4)	2.873(2)	2.891(1)	2.872(1)	2.910(1)
S···H−C distance between 1D chains/Å	2.894(3)	2.705(2)	3.024(1)	2.982(1)	3.162(1)
S···H−C distance between solvent and Fe unit/Å	3.081(2)	3.231(3)			
	3.434(1)	3.022(1)	2.775(1)	2.744(1)	3.165(1)
	2.985(1)	3.044(2)			

upon cooling, from 3.514 cm^3 K mol^{-1} at 300 K, to a plateau of 0.021 cm^3 K mol^{-1} between 100 and 2 K, with $T_{1/2}$ of ca. 140 K. Complex ***i*-PrOH** is in hs state at 300 K, with a $\chi_M T$ value of 3.450 cm^3 K mol^{-1}. As temperature decreases to 160 K, the $\chi_M T$ value begins to decrease rapidly and reaches a plateau of 0.046 cm^3 K mol^{-1} from 110 to 2 K. This feature indicates that complex ***i*-PrOH** displays a one-step complete and abrupt spin transition. Complex **CH_2Cl_2** displays a gradual spin transition, with temperature-dependent behavior similar to that of ***n*-PrOH**, and the $T_{1/2}$ is ca. 146 K. However, the ls state plateau with $\chi_M T$ value of 0.215 cm^3 K mol^{-1} is a little higher than normal one, which most probably arises from residual hs-Fe^{II} population or paramagnetic impurities. Complex **$CHCl_3$** undergoes a gradual, incomplete spin transition from a $\chi_M T$ value of 3.432 cm^3 K mol^{-1} at 300 K to a value of 2.165 cm^3 K mol^{-1} at 50 K. After a 25 K wide plateau, a further decrease of the $\chi_M T$ value is observed, which is most possibly due to the zero-field effect of the residual hs-Fe^{II} ions.[24] Interestingly, the complex **MeCN** is paramagnetic in the whole temperature range, completely different from other complexes. This difference may originate from the different crystal packing and intermolecular interactions.

The magnetic measurements were also carried out on the products after exposure to various guest vapors, as shown in Figure 6. The SCO behavior of samples **MeOH** and **EtOH** obtained by solvent exchanges from yellow crystals of ***n*-PrOH**, ***i*-PrOH**, **CH_2Cl_2**, **$CHCl_3$**, and **MeCN** are almost the same as those of **MeOH** and **EtOH** obtained by recrystallization or those of MeOH- and EtOH-absorbed **pI**. Slight differences are observed for **CH_2Cl_2** and **$CHCl_3$**, which differ in sample preparation, the crude powder exchanged from **MeOH** or **EtOH** (sample a) and the crystalline materials recrystallized from **pI** (sample b), respectively. For **$CHCl_2$**, the temperature-dependent bahavior and $\chi_M T$ values above 200 K are almost the same for samples a and b; however, an increase of SCO completeness is observed from an incomplete transition (sample b) to a complete SCO behavior (sample a), though elemental analysis and X-ray powder diffraction data of sample a are consistent with those of sample b. Similar completeness-enhancement was also observed for **$CHCl_3$**. Such differences in the magnetic properties between samples a and b might result from slightly different chemical compositions or impurities and other kinds of defects in the crystal lattice, for example, residual methanol or ethanol molecules, which cannot be detected by PXRD and elemental analysis due to the low sensitivity of these techniques.[25]

Crystallographic Studies. Single-crystal X-ray diffraction data were collected at various temperatures in order to correlate the structures with different SCO states identified by the magnetic studies. Overall, the basic molecular moiety of these complexes, as expected, is the distorted octahedral Fe^{II} core chelated by one tetradentate tpa ligand and two NCS^- groups. It is the encapsulated guest molecules that significantly perturb the intercomplex interactions and modify ligand field energies at the iron(II) sites via hydrogen-bond interactions between the complex and solvent molecules, and, more importantly, determine the SCO behavior and associated magnetic properties of the complexes.

Complex **EtOH** is isostructural to complex **MeOH**,[22c] belonging to the same space group $P\bar{1}$. Two crystallographically distinct complex units, $[Fe_A(tpa)(NCS)_2]\cdot EtOH$ (Fe_A unit) and $[Fe_B(tpa)(NCS)_2]$ (Fe_B unit), respectively, were found in each asymmetric unit of these complexes.

Crystal data of **EtOH** were collected at 295, 230, and 150 K, respectively, in order to correlate the structures at different temperatures with the different magnetic phases of the one-step-like spin transition, which is different from the two-step spin transitions of the isostructural complexes, **pIV** and **MeOH**, as revealed by the magnetic studies shown in Figure 5. At 295 K, the Fe−N bond lengths range from 2.235(3) to 2.030(5) Å with averages of 2.118 and 2.146 Å for the Fe_A and Fe_B units, respectively. Both values are in the range expected for a hs Fe^{II}−N bond, and the spin state is consistent with the room-temperature magnetic susceptibility. Upon cooling, both Fe−N bond lengths of Fe_A and Fe_B units show sizable decrease to 2.015 and 2.060 Å, respectively, at 230 K. At this temperature, the average Fe−N bond lengths are shorter than a normal hs Fe^{II}−N bond but longer than a ls one, which in fact are reasonable values for intermediate-phase (ip) Fe^{II} ions. At 150 K, the corresponding values are 1.962 and 1.965 Å for Fe_A and Fe_B units, respectively, showing that all Fe^{II} ions are in ls states. An hs-Fe_A/hs-Fe_B ↔ ls-Fe_A/ls-Fe_B one-step spin transition is thus suggested in this temperature range. In other words, no intermediate hs−ls phase is observed, which was the typical characteristic for its isostructural complexes, **pIV** and **MeOH**. However, it should be noted that the two distinct complex units of Fe_A and Fe_B cannot display the same SCO behavior crystallographically[26] and the spin-transition process of **EtOH** should contain two successive steps, which has been already discussed for the isostructural **pIV** and **MeOH**. However, the multiple steps are not resolved

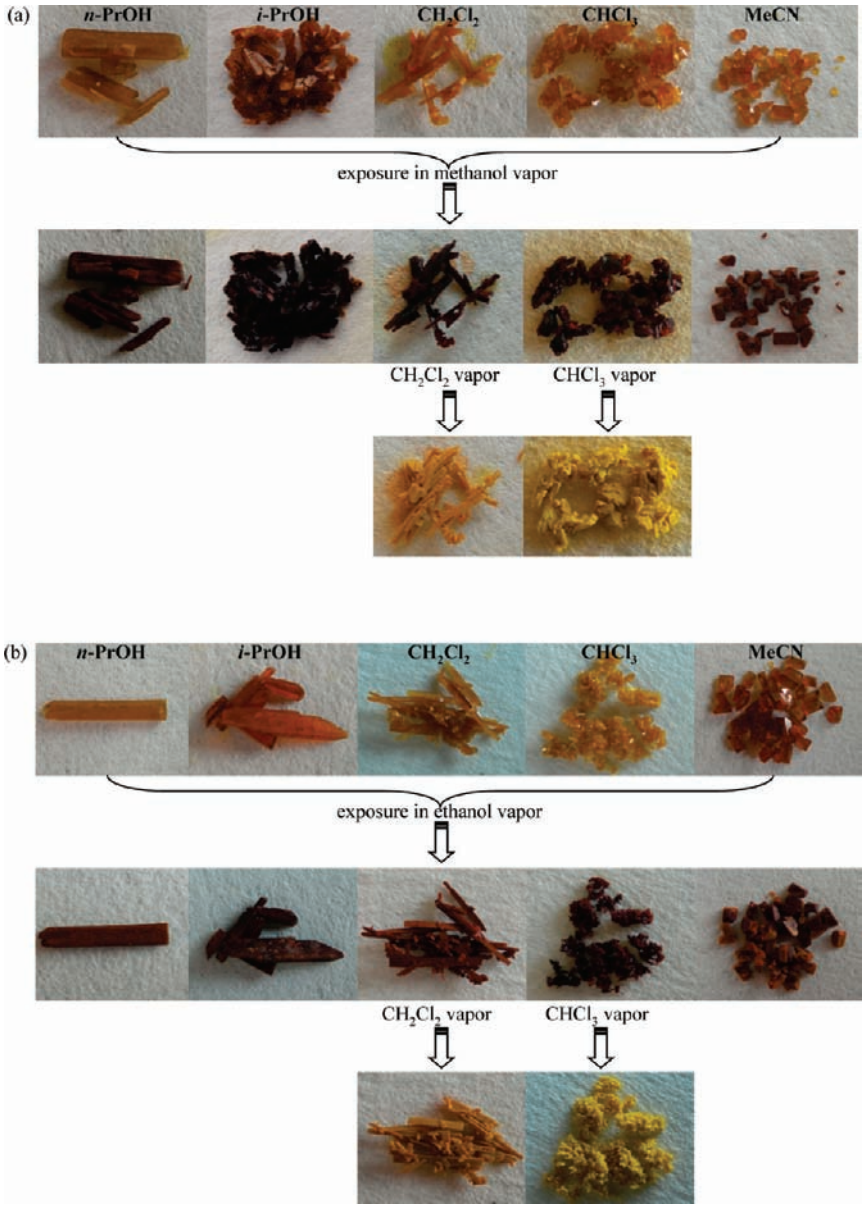

Figure 3. Color changes for crystals of ***n*-PrOH**, ***i*-PrOH**, **CH_2Cl_2**, **$CHCl_3$**, and **MeCN** from yellow to red upon exposure to (a) methanol and (b) ethanol vapor, respectively, and then recover to yellow while exposing the associating samples to methylene dichloride and chloroform vapor.

macroscopically in **EtOH**, which exhibits a one-step-like spin conversion revealed by magnetic studies.

Both of the propanol complexes, ***n*-PrOH** and ***i*-PrOH**, crystallize in the monoclinic space group $P2_1/c$. Their asymmetric units contain one complete $[Fe(tpa)(NCS)_2]$ complex and an associated solvent molecule, n-propanol and iso-propanol, respectively. At 240 K, all Fe^{II} ions persist in the hs state with average Fe−N bond lengths of 2.167 and 2.166 Å for ***n*-PrOH** and ***i*-PrOH**, respectively. Upon cooling to 104 K, the corresponding values decrease to 1.977 and 1.974 Å for ***n*-PrOH** and ***i*-PrOH**, respectively. The Fe−N bonds shrink by an average value of approximately 0.2 Å for the two complexes during the transition from hs to ls state, indicating that the spin transitions are complete. In fact, the coordination environments of the Fe^{II} sites at hs and ls states in ***n*-PrOH** and ***i*-PrOH** are very similar; the variations for the geometries have been quantified by using the octahedral distortion parameter,[27,28] Σ, a parameter featuring the angular deviation from octahedral geometry (calculated by sum of the deviation of each of the 12 *cis* angles from 90°). A smaller Σ value is generally expected to associate with a stronger ligand field and, therefore, stabilizes the ls state of metal ion, while the opposite holds true for an hs state. Here, the Σ values are 98.4° (hs) and 50.6° (ls) and 99.9° (hs) and 51.6° (ls), for ***n*-PrOH** and ***i*-PrOH**, respectively, at 240 and 104 K, indicating a stronger ligand field at low temperature than that at high temperature.

Complex **CH_2Cl_2** crystallizes in the orthorhombic space group $Pna2_1$. The asymmetric unit contains three crystallographically distinct complex $[Fe(tpa)(NCS)_2]$ species, herein denoted as Fe_A, Fe_B, and Fe_C, respectively, each featuring hydrogen-bond interaction with a different guest CH_2Cl_2 molecule. At 230 K, the average Fe−N bond lengths are 2.174, 2.152, and 2.157 Å for Fe_A, Fe_B, and Fe_C units, respectively, indicating that all Fe^{II} ions are in hs states. Upon cooling to 104 K, the average Fe−N bond lengths of Fe_A and Fe_C units decrease to

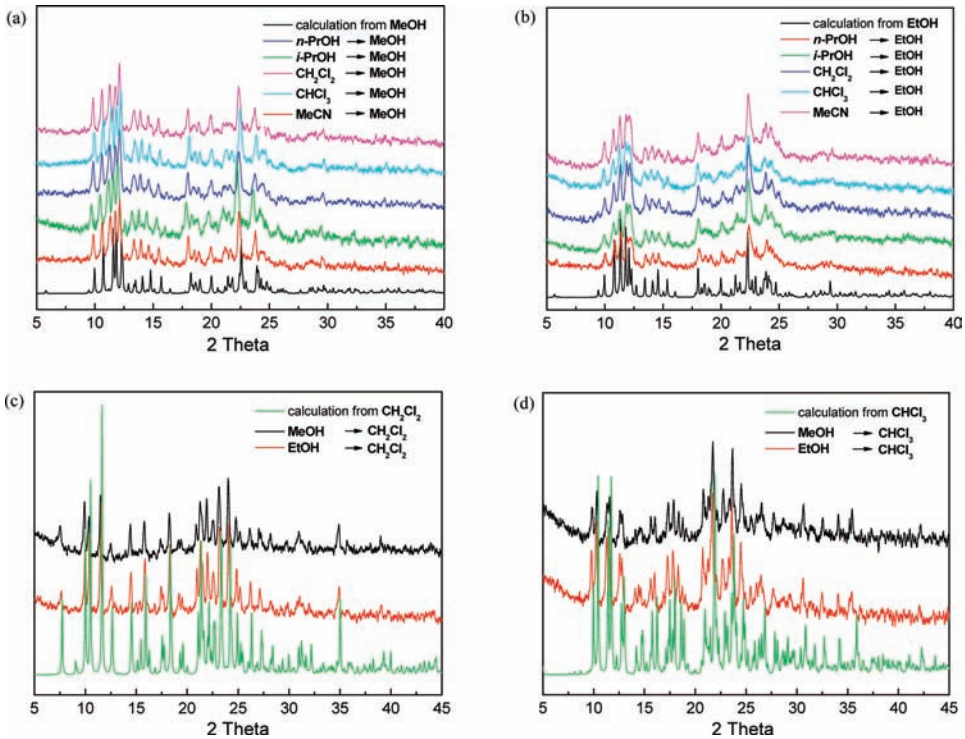

Figure 4. PXRD patterns of solvate samples after exposure in (a) methanol, (b) ethanol, (c) methylene chloride, and (d) chloroform vapor, respectively, compared to the calculated results from single-crystal data of associating solvate complexes.

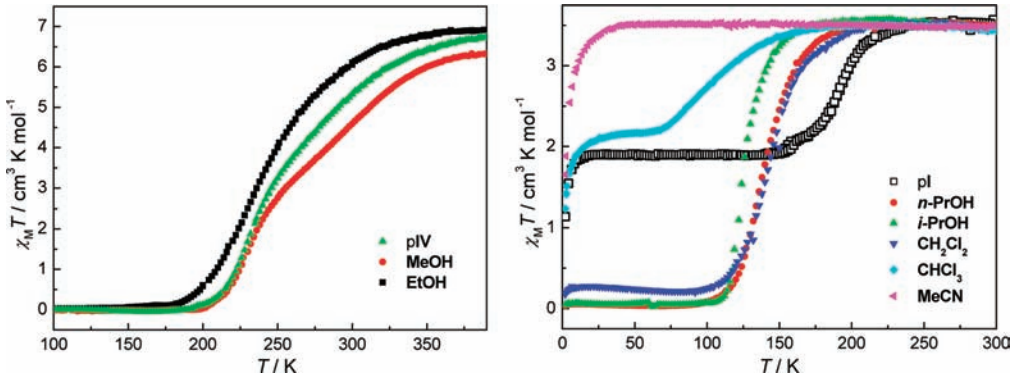

Figure 5. $\chi_M T$ versus T plots for **pIV**, **MeOH**, and **EtOH** (per Fe_2 unit, left), and **pI**, ***n*-PrOH**, ***i*-PrOH**, **CH_2Cl_2**, **$CHCl_3$**, and **MeCN** (per Fe unit, right), respectively.

1.966 and 1.969 Å, respectively, while that of Fe_B decreases to 1.984 Å, which is slightly longer than the typical ls Fe^{II}−N bond length, accompanied by approximately 6% hs concentration revealed by magnetic studies at this temperature.

Complex **$CHCl_3$** crystallizes in the monoclinic space group $P2_1/c$, and the crystal data were collected at 240 and 104 K. Two crystallographically distinguishable Fe^{II} units, Fe_A and Fe_B, respectively, are found in the asymmetric unit, one of which (the Fe_A unit) forming a strong S···H−C hydrogen bond with a $CHCl_3$ molecule (Table 7). At 240 K, both of the Fe_A and Fe_B units are in the hs state, with an average Fe−N bond length of 2.168 and 2.174 Å, respectively. Upon cooling to 104 K, the average Fe_A−N bond length shows a sizable decrease to 2.087 Å, which is a reasonable value for an ip-Fe^{II} ion, whereas the corresponding value associated with the Fe_B site remains unchanged, indicating an hs-Fe_A/hs-Fe_B to ip-Fe_A/hs-Fe_B transition in this temperature range.

Complex **MeCN** crystallizes in the orthorhombic space group $P2_12_12_1$. At 150 K, the average Fe−N bond length is 2.167 Å, suggesting that the Fe^{II} center in **MeCN** is in hs state. On the other hand, the FeN_6 coordination octahedron is highly distorted with an octahedral distortion parameter (Σ) value of 105.4 at 150 K, which is larger than those of other solvate complexes, indicating a weaker ligand field in **MeCN**, and as a result, **MeCN** retains in hs state.

The main differences between $[Fe(tpa)(NCS)_2]\cdot X$ (***n*-PrOH**, ***i*-PrOH**, **CH_2Cl_2**, **$CHCl_3$** and **MeCN**) and $[Fe(tpa)(NCS)_2]_2\cdot Y$ (**MeOH** and **EtOH**) are in their crystal-packing patterns, as is shown in Figure 7. The molecular packing of **MeOH** and **EtOH** can be viewed as 2D layers stacking along the *c* axis containing mutually

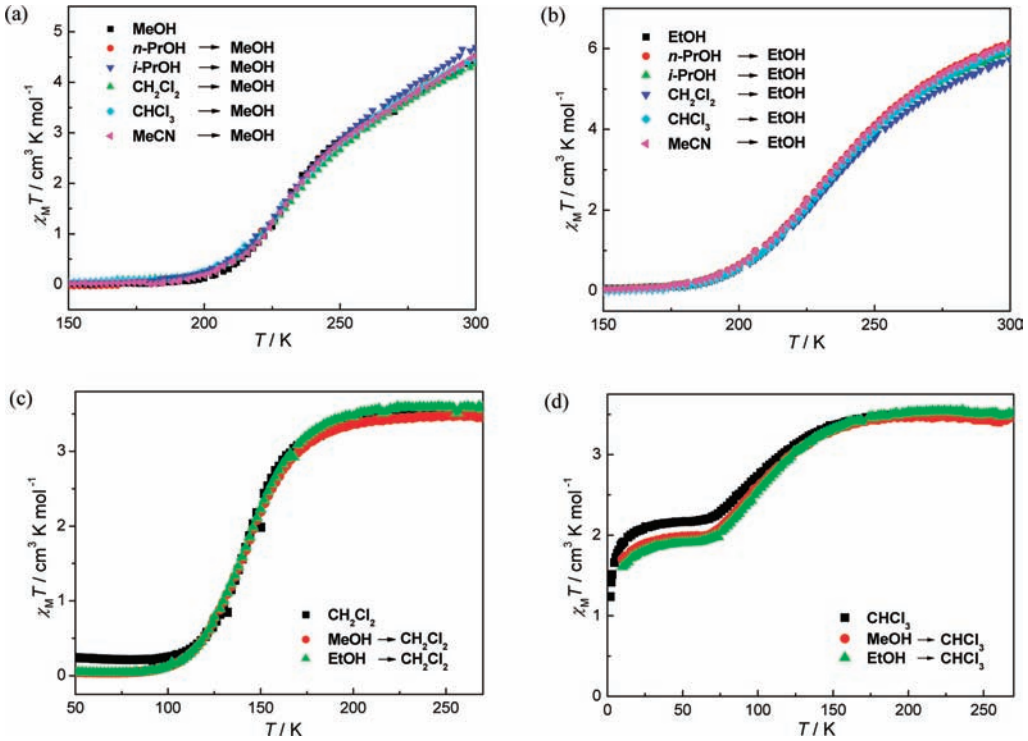

Figure 6. (a, b) $\chi_M T$ versus T plots (per Fe_2 unit) of **MeOH** and **EtOH** obtained by exposure of ***n*-PrOH**, ***i*-PrOH**, CH_2Cl_2, $CHCl_3$, and **MeCN** crystals in methanol and ethanol vapor, respectively. (c, d) $\chi_M T$ versus T plots (per Fe unit) for CH_2Cl_2 and $CHCl_3$ obtained by exposure of **MeOH** and **EtOH** crystals in methylene chloride and chloroform vapor, respectively. Magnetic susceptibilities of single-crystal samples are presented for comparison (■).

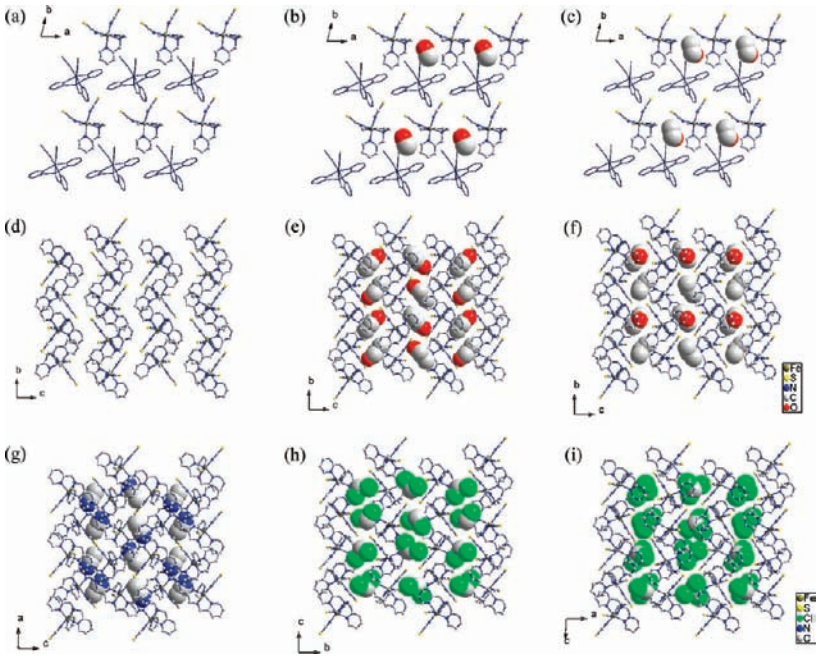

Figure 7. Crystal packing diagrams of (a) p**IV**, (b) **MeOH**, (c) **EtOH**, (d) p**I**, (e) ***n*-PrOH**, (f) ***i*-PrOH**, (g) **MeCN**, (h) CH_2Cl_2 and (i) $CHCl_3$, respectively. For a−c, Fe_A units are displayed in capped stick form and Fe_B in ball and stick form.

parallel chains of Fe_A and Fe_B units in the *ab* plane, similar to those of p**IV** (Figures 7a−c).

For **EtOH**, ethanol molecules occupy the voids between Fe_A and Fe_B layers and contact with Fe_A units by S···H−O hydrogen bond with distances of 2.900(1) and 2.316(1) Å at 295 and 150 K, respectively. While $\pi-\pi$ interactions within Fe_A and Fe_B layers are uninformative with centroid-to-centroid separations exceeding the van der Waals distance, S···H−C hydrogen bonding interactions are found within and between the Fe_A and Fe_B layers, and the corresponding structural parameters

Table 8. Comparison of Magnetic and Solvent Properties[30]

complex	$T_{1/2}$/K	residual hs population /%	characteristic of SCO	solvent volume/Å^3	dipole/D	dielectric constant/20 °C	polarity (water 100)
pI	192	53	continuous				
pIV	293, 230	0	two steps				
MeOH	303, 229	0	two steps	34.1	1.7	32.6	76.2
EtOH	242	0	one-step-like	49.8	1.7	22.4	65.4
***n*-PrOH**	140	0	continuous	65.7	1.7	20.1	61.7
***i*-PrOH**	125	0	abrupt	65.2	1.66	18.3	54.6
CH_2Cl_2	143	6	continuous	56.3	1.8	9.1	30.9
$CHCl_3$	102	62	continuous	69.9	1.1	4.8	25.9
MeCN		100	high spin	45.9	3.2	37.5	46

at various temperatures are shown in Table 5 with comparison of those of p**IV** and **MeOH**.

For $[Fe(tpa)(NCS)_2]\cdot X$, the corrugated complex chains are stabilized by both $\pi-\pi$ interactions and S···H−C hydrogen bonds between adjacent complex units and are arranged parallel to form two-dimensional layers, which are isostructural to the nonsolvent polymorphs p**I**, as is shown in Figure 7d−i. Solvent molecules occupy the channel between the complex chains and contact with the complex units by S···H−O or S···H−C hydrogen bonds. Those intermolecular interaction variations upon temperature change are presented in Tables 6 and 7, respectively, comparing with the corresponding values of p**I**.

The structural parameters discussed above show that encapsulation or changing solvent molecules do not obviously alternate the 2D supramolecular arrays and layer-stacking structures in $[Fe(tpa)(NCS)_2]\cdot X$ and $[Fe(tpa)(NCS)_2]_2\cdot Y$, respectively, thus giving similar intermolecular interactions between the complex units in each group. However, they clearly differ in details in giving different chemical environments around the SCO centers, which are responsible for the relatively different SCO properties observed for these isostructural complexes of $[Fe(tpa)(NCS)_2]\cdot X$ and $[Fe(tpa)(NCS)_2]_2\cdot Y$, respectively.

Solvent Effect. Strong correlations between the nature of solvents and SCO behaviors of solvate $[Fe(tpa)(NCS)_2]$ family have been established, as summarized in Table 8. First of all, the encapsulation of solvent molecules is expected to alternate the lattice phonon distribution resulting in different crystal packing modes and intermolecular interactions.[13b] In the present cases, methanol and ethanol molecules seem to stabilize the crystal packing mode of p**IV**, while the other solvents are p**I**-favorable. The difference between the crystal packing styles is believed to cause color difference at room temperature between the p**I**-like (yellow) and the p**IV**-like (red) complexes, and, more importantly, results in different SCO behavior occurring in two temperature ranges, $T_{1/2} < 200$ K for p**I**-like complexes and $T_{1/2} > 200$ K for p**IV**-like complexes, respectively (Figure 5). Moreover, the introduction of hydrogen-bond interactions between guest molecules and complex units obviously enhances the ligand field of the involved complex unit, resulting in an increase of critical transition temperature. For example, the encapsulation of methanol molecules introduces strong S···H−O interactions between the Fe_A complex and methanol molecules, which enhance ligand field exerted on the Fe_A SCO center,[20c] resulting in an increase of $T_{1/2}(Fe_A)$ of the associated SCO behavior from 293 K (nonguest complex p**IV**) to 303 K, while the transition of other half SCO center occurring at a lower temperature range, associated with the Fe^{II} site (Fe_B) without hydrogen-bond interactions with methanol molecules, remains unchanged. Meanwhile, the sizes of solvent molecules residing in the channels or cavities in the supramolecular structures also influence the SCO behavior, which may prevent the contract of the crystal lattice upon the transition from hs to ls state, thus decreasing the transition temperature ("inner pressure" argument).[20d] The encapsulation of ethanol molecules gives similar S···H−O hydrogen-bond interactions as those of MeOH; however, the structurally two-step SCO behavior decays to a one-step-like curve, along with the disappearance of the hs−ls intermediate state as well as a decrease of critical temperature from 260 to 246 K (Figure 5, left).

In contrast, the solvates in $[Fe(tpa)(NCS)_2]\cdot X$, which share a similar 2-D layer structure as well as p**I**, show rather different SCO, and the solvent influences are more complex than those of $[Fe(tpa)(NCS)_2]_2\cdot Y$. At a first glance, the introduction of n-propanol and iso-propanol molecules into the 2D supramolecular array of p**I** lead to significant changes in the SCO behavior from hs-to-ip half SCO for p**I** to hs-to-ls complete SCO for ***n*-PrOH** and ***i*-PrOH**, suggesting enhancement of the ligand field exerting on the Fe^{II} center. As discussed above, the inner pressure is strongly related to the guest volume. In the present case, the n-propanol and iso-propanol molecules share similar volumes, and the transition temperatures of the associating SCO behavior are almost the same, except that the abruptness is slightly different; that is, complex ***n*-PrOH** shows a gradual SCO while ***i*-PrOH** undergoes SCO more rapidly (Figure 5, right), which may be related to the difference in the anisotropic inner pressures generated by the rodlike n-propanol and disklike iso-propanol molecules. It should be noted, however, that **CH_2Cl_2**, **$CHCl_3$**, and **MeCN** are in the reverse of the "inner pressure" argument above, of which the solvent volumes are similar to or even smaller than those of the propanol analogues,[20d,29] ***n*-PrOH** and ***i*-PrOH**: decays of the completeness of associating spin transition are observed. Indeed, the electronic effect of solvent molecules including polarity and polarizability may also take part in the electrostatic contributions on spin transition.[20e] However, none of the variability of guest parameters, such as dipole, polarity, and dielectric constant,[30] shows any obvious correlation with the $T_{1/2}$ values or the nature of SCO in the present cases. Quantitative analysis of the electrostatic contributions of those solvent molecules on spin transition by ab initio calculations[31,32] is thus required in our future research.

■ CONCLUSIONS

We have reported an interesting SCO system showing reversible and irreversible guest molecule exchanges in the solid state that are triggered by the associating solvent vapor, of which distinct structural transformations have been confirmed by X-ray crystallographic and PXRD studies as well as SCO behavior

transformations revealed by magnetic studies. The structures of yellow complexes (***n*-PrOH**, ***i*-PrOH**, **CH_2Cl_2**, **$CHCl_3$**, and **MeCN**) and red ones (**MeOH** and **EtOH**) mainly differ from the molecular packing patterns, which are isostructural to the nonsolvent polymorphs p**I** and p**IV**, respectively. The two types of complexes are highly sensitive to specific solvent vapors, i.e., methanol and ethanol for ***n*-PrOH**, ***i*-PrOH**, **CH_2Cl_2**, **$CHCl_3$**, and **MeCN**, and methylene chloride and chloroform for **MeOH** and **EtOH**, respectively. Solvent vapor molecules are able to completely replace the original guest molecules, thus greatly changing intra- and intermolecular interactions, and, more importantly, acutely alter the SCO properties. Detailed studies on crystal structures and magnetic properties have unveiled a remarkable solvent dependence of SCO behavior of these complexes that is related to the nature of solvents. The present study contributes a vivid example to fine-tune and optimize materials' properties via systematic structural perturbation. Moreover, the crystalline transformations induced by in situ solvent exchange provide a significant step toward tuning magnetic properties on the molecular scale, which is a long sought-after goal in bistable materials research.

■ ASSOCIATED CONTENT

Supporting Information. Crystallographic information in CIF format. This material is available free of charge via the Internet at http://pubs.acs.org.

■ AUTHOR INFORMATION

Corresponding Author
*E-mail: taojun@xmu.edu.cn.

■ ACKNOWLEDGMENT

This work was supported by the NNSF of China (Grants 90922012, 20971106, and 21021061), the NSF of Fujian Province for Distinguished Young Scientists (Grant 2009J06006), and the National Basic Research Program of China (973 program, Grant 2007CB815301).

■ REFERENCES

(1) (a) Kitagawa, S.; Kitaura, R.; Noro, S. *Angew. Chem., Int. Ed.* **2004**, *43*, 2334. (b) Long, J. R.; Yaghi, O. M. *Chem. Soc. Rev.* **2009**, *38*, 1213. (c) Tranchemontagne, D. J.; Mendoza-Cortes, J. L.; O'Keeffe, M.; Yaghi, O. M. *Chem. Soc. Rev.* **2009**, *38*, 1257.

(2) (a) Kitaura, R.; Kitagawa, S.; Kubota, Y.; Kobayashi, T.; Kindo, L.; Mita, Y.; Matsuo, A.; Kobayashi, M.; Chang, H.-C.; Ozawa, T.; Suzuki, M.; Sakata, M.; Takata, M. *Science* **2002**, *298*, 2358. (b) Matsuda, R.; Kitaura, R.; Kitagawa, S.; Kubota, Y.; Belosludov, R. V.; Kobayashi, T. C.; Sakamoto, H.; Chiba, T.; Takata, M.; Kawazoe, Y.; Mita, Y. *Nature* **2005**, *436*, 238.

(3) (a) Yaghi, O. M.; Li, G. M.; Li, H. L. *Nature* **1995**, *378*, 703. (b) Chae, H. K.; Siberio-Perez, D. Y.; Kim, J. H.; Go, Y. B.; Yaghi, O. M. *Nature* **2004**, *427*, 523.

(4) Albrecht, M.; Lutz, M.; Spek, A. L.; van Koten, G. *Nature* **2000**, *406*, 970.

(5) (a) Ghosh, S. K.; Zhang, J.-P.; Kitagawa, S. *Angew. Chem., Int. Ed.* **2007**, *46*, 7965. (b) Hu, C.; Englert, U. *Angew. Chem., Int. Ed.* **2006**, *45*, 3457. (c) Nagarathinam, M.; Vittal, J. J. *Angew. Chem., Int. Ed.* **2006**, *45*, 4337. (d) Wu, C.-D.; Lin, W. *Angew. Chem., Int. Ed.* **2005**, *44*, 1958. (e) Liu, Q.-K.; Ma, J.-P.; Dong, Y.-B. *J. Am. Chem. Soc.* **2010**, *132*, 7005.

(6) (a) Vittal, J. J. *Coord. Chem. Rev.* **2007**, *251*, 1781. (b) Kawano, M.; Fujita, M. *Coord. Chem. Rev.* **2007**, *251*, 2592.

(7) Huang, Z.; White, P. S.; Brookhart, M. *Nature* **2010**, *465*, 598.

(8) (a) Nihei, M.; Han, L.; Oshio, H. *J. Am. Chem. Soc.* **2007**, *129*, 5312. (b) Amoore, J. J. M.; Kepert, C. J.; Cashion, J. D.; Moubaraki, B.; Neville, S. M.; Murray, K. S. *Chem.—Eur. J.* **2006**, *12*, 8220. (c) Amoore, J. J. M.; Neville, S. M.; Moubaraki, B.; Iremonger, S. S.; Murray, K. S.; Létard, J.-F.; Kepert, C. J. *Chem. —Eur. J.* **2010**, *16*, 1973. (d) Han, Y.-F.; Jia, W.-G.; Lin, Y.-J.; Jin, G.-X. *Angew. Chem., Int. Ed.* **2009**, *48*, 6234. (e) Davis, A. V.; Raymond, K. N. *J. Am. Chem. Soc.* **2005**, *127*, 7912. (f) Mugridge, J. S.; Bergman, R. G.; Raymond, K. N. *Angew. Chem., Int. Ed.* **2010**, *49*, 3635.

(9) Caira, M. R.; Nassimbeni, L. R. In *Comprehensive Supramolecular Chemistry*; Atwood, J. L., Davies, J. E. D., MacNicol, D. D., Vögtle, F., Eds.; Elsevier Science: Oxford, 1996; Vol. 6.

(10) (a) Wang, Z.; Chen, G.; Ding, K. *Chem. Rev.* **2009**, *109*, 322. (b) Pluth, M. D.; Bergman, R. G.; Raymond, K. N. *Science* **2007**, *316*, 85. (c) Yoshizawa, M.; Tamura, M.; Fujita, M. *Science* **2006**, *312*, 251. (d) Kang, J. M.; Hilmersson, G.; Santamaria, J.; Rebek, J. *J. Am. Chem. Soc.* **1998**, *120*, 3650. (e) Hasting, C. J.; Fiedler, D.; Bergman, R. G.; Raymond, K. N. *J. Am. Chem. Soc.* **2008**, *130*, 10977. (f) Yoshizawa, M.; Takeyama, Y.; Okano, T.; Fujita, M. *J. Am. Chem. Soc.* **2003**, *125*, 3243.

(11) (a) Duan, Z.; Zhang, Y.; Zhang, B.; Zhu, D. *J. Am. Chem. Soc.* **2009**, *131*, 6934. (b) Ono, K.; Yoshizawa, M.; Akita, M.; Kato, T.; Tsunobuchi, Y.; Ohkoshi, S.; Fujita, M. *J. Am. Chem. Soc.* **2009**, *131*, 2782. (c) Cheng, X.-N.; Zhang, W.-X.; Chen, X.-M. *J. Am. Chem. Soc.* **2007**, *129*, 15738. (d) Cheng, X.-N.; Zhang, W.-X.; Lin, Y.-Y.; Zheng, Y.-Z.; Chen, X.-M. *Adv. Mater.* **2007**, *19*, 1494. (e) Zhang, W.-X.; Xue, W.; Chen, X.-M. *Inorg. Chem.* **2011**, *50*, 309.

(12) (a) Wang, P.; Ma, J.-P.; Dong, Y.-B.; Huang, R.-Q. *J. Am. Chem. Soc.* **2007**, *129*, 10620. (b) Wang, P.; Ma, J.-P.; Dong, Y.-B. *Chem.—Eur. J.* **2009**, *15*, 10432. (c) Jiang, Y.-Y.; Ren, S.-K.; Ma, J.-P.; Liu, Q.-K.; Dong, Y.-B. *Chem.—Eur. J.* **2009**, *15*, 10742. (d) Dalgarno, S. J.; Tucker, S. A.; Bassil, D. B.; Atwood, J. L. *Science* **2005**, *309*, 2037. (e) Dong, Y.-B.; Wang, P.; Ma, J.-P.; Zhao, X.-X.; Wang, H.-Y.; Tang, B.; Huang, R.-Q. *J. Am. Chem. Soc.* **2007**, *129*, 4872. (f) McManus, G. J.; Perry, J. J.; Perry, M.; Wagner, B. D.; Zaworotko, M. J. *J. Am. Chem. Soc.* **2007**, *129*, 9094.

(13) (a) Shultz, D. A. In *Magnetism: Molecules to Materials II*; Miller, J. S., Drillon, M., Eds.; Wiley-VCH: Weinheim, Germany, 2001; p 281. (b) Gütlich, P.; Goodwin, H. A. *Top. Curr. Chem.* **2004**, *234*, 1. (c) Kahn, O.; Launay, J. P. *Chemtronics* **1988**, *3*, 140. (d) Sato, O.; Iyoda, T.; Fujishima, A.; Hashimoto, K. *Science* **1996**, *272*, 704. (e) Gütlich, P.; Garcia, Y.; Woike, T. *Coord. Chem. Rev.* **2001**, *219—221*, 839. (f) Sato, O.; Tao, J.; Zhang, Y.-Z. *Angew. Chem., Int. Ed.* **2007**, *46*, 2152.

(14) Bousseksou, A.; Molnár, G.; Matouzenko, G. *Eur. J. Inorg. Chem.* **2004**, 4353.

(15) Sorai, M.; Ensling, J.; Hasselbach, K. M.; Gütlich, P. *Chem. Phys.* **1977**, *20*, 197.

(16) (a) Létard, J. F.; Guionneau, P.; Goux-Capes, L. *Top. Curr. Chem.* **2004**, *235*, 221. (b) Murray, K. S.; Kepert, C. J. *Top. Curr. Chem.* **2004**, *233*, 195. (c) Kepenekian, M.; Guennic, B. L.; Robert, V. *J. Am. Chem. Soc.* **2009**, *131*, 11498.

(17) (a) Halder, G. J.; Kepert, C. J. *Aust. J. Chem.* **2006**, *59*, 597. (b) Neville, S. M.; Leita, B. A.; Halder, G. J.; Kepert, C. J.; Moubaraki, B.; Létard, J. F.; Murray, K. S. *Chem.—Eur. J.* **2008**, *14*, 10123. (c) Zhang, W.; Zhao, F.; Liu, T.; Yuan, M.; Wang, Z.-M.; Gao, S. *Inorg. Chem.* **2007**, *46*, 2541. (d) Hostettler, M.; Törnroos, K. W.; Chernyshov, D.; Vangdal, B.; Bürgi, H.-B. *Angew. Chem., Int. Ed.* **2004**, *43*, 4589. (e) Leita, B. A.; Neville, S. M.; Halder, G. J.; Moubaraki, B.; Kepert, C. J.; Létard, J.-F.; Murray, K. S. *Inorg. Chem.* **2007**, *46*, 8784.

(18) Inokuma, Y.; Arai, T.; Fujita, M. *Nature Chem.* **2010**, *2*, 780.

(19) Halder, G. J.; Kepert, C. J.; Moubaraki, B.; Murray, K. S.; Cashion, J. D. *Science* **2002**, *298*, 1762.

(20) (a) Halder, G. J.; Chapman, K. W.; Neville, S. M.; Moubaraki, B.; Murray, K. S.; Létard, J.-F.; Kepert, C. J. *J. Am. Chem. Soc.* **2008**, *130*, 17552. (b) Neville, S. M.; Halder, G. J.; Chapman, K. W.; Duriska, M. B.; Southon, P. D.; Cashion, J. D.; Létard, J.-F.; Moubaraki, B.; Murray, K. S.; Kepert, C. J. *J. Am. Chem. Soc.* **2008**, *130*, 2869. (c) Neville, S. M.; Moubaraki, B.; Murray, K. S.; Kepert, C. J. *Angew. Chem., Int. Ed.* **2007**, *46*, 2059. (d) Southon, P. D.; Liu, L.; Fellows, E. A.; Price, D. J.;

Halder, G. J.; Chapman, K. W.; Moubaraki, B.; Murray, K. S.; Létard, J.-F.; Kepert, C. J. *J. Am. Chem. Soc.* **2009**, *131*, 10998. (e) Neville, S. M.; Halder, G. J.; Chapman, K. W.; Duriska, M. B.; Moubaraki, B.; Murray, K. S.; Kepert, C. J. *J. Am. Chem. Soc.* **2009**, *131*, 12106.

(21) Ohba, M.; Yoneda, K.; Agustí, G.; Muñoz, M. C.; Gaspar, A. B.; Real, J. A.; Yamasaki, M.; Ando, H.; Nakao, Y.; Sakaki, S.; Kitagawa, S. *Angew. Chem., Int. Ed.* **2009**, *48*, 4767.

(22) (a) Højland, F.; Toftlund, H.; Yde-Andersen, S. *Acta Chem. Scand.* **1983**, *A37*, 251. (b) Paulsen, H.; Grünsteudel, H.; Meyer-Klaucke, W.; Gerdan, M.; Grünsteudel, H. F.; Chumakov, A. I.; Rüffer, R.; Winkler, H.; Toftlund, H.; Trautwein, A. X. *Eur. Phys. J.* **2001**, *B23*, 463. (c) Li, B.; Wei, R.-J.; Tao, J.; Huang, R.-B.; Zheng, L.-S.; Zheng, Z. *J. Am. Chem. Soc.* **2010**, *132*, 1558. (d) Wei, R.-J.; Li, B.; Tao, J.; Huang, R.-B.; Zheng, L.-S.; Zheng, Z. *Inorg. Chem.* **2011**, *50*, 1170.

(23) Sheldrick, G. M. *Acta Crystallogr.* **2008**, *A64*, 112.

(24) (a) Moliner, N.; Muñoz, M. C.; Létard, S.; Salmon, L.; Tuchagues, J.-P.; Bousseksou, A.; Real, J. A. *Inorg. Chem.* **2002**, *41*, 6997. (b) Niel, V.; Gaspar, A. B.; Muñoz, M. C.; Abarca, B.; Ballesteros, R.; Real, J. A. *Inorg. Chem.* **2003**, *42*, 4782.

(25) Bonnet, S.; Molnár, G.; Costa, J. S.; Siegler, M. A.; Spek, A. L.; Bousseksou, A.; Fu, W. T.; Gamez, P.; Reedijk, J. *Chem. Mater.* **2009**, *21*, 1123.

(26) Breuning, E.; Ruben, M.; Lehn, J.-M.; Renz, F.; Garcia, Y.; Ksenofontov, V.; Gütlich, P.; Wegelius, E.; Rissanen, K. *Angew. Chem., Int. Ed.* **2000**, *39*, 2504.

(27) Guionneau, P.; Marchivie, M.; Bravic, G.; Létard, J. F.; Chasseau, D. *J. Mater. Chem.* **2002**, *12*, 2546.

(28) Guionneau, P.; Marchivie, M.; Bravic, G.; Létard, J. F.; Chasseau, D. *Top. Curr. Chem.* **2004**, *234*, 97.

(29) Webster, C. E.; Drago, R. S.; Zerner, M. C. *J. Am. Chem. Soc.* **1998**, *120*, 5509.

(30) Smallwood, I. M. *Handbook of Organic Solvent Properties*; Amold: London, 1996.

(31) Kepenekian, M.; Le Guennic, B.; Robert, V. *J. Am. Chem. Soc.* **2009**, *131*, 11498.

(32) Kepenekian, M.; Le Guennic, B.; Robert, V. *Phys. Rev.* **2009**, *B79*, 094428/1.